

# Collective modes in ordered Mott systems: dynamical mean-field study

D. Geffroy,<sup>1,2</sup> J. Kaufmann,<sup>2</sup> A. Hariki,<sup>2</sup> P. Gunacker,<sup>2</sup> A. Hausoel,<sup>3</sup> and J. Kuneš<sup>2,4</sup>

<sup>1</sup>*Department of Condensed Matter Physics, Faculty of Science,  
Masaryk University, Kotlářská 2, 611 37 Brno, Czechia*

<sup>2</sup>*Institute for Solid State Physics, TU Wien, 1040 Vienna, Austria*

<sup>3</sup>*Institute for Theoretical Physics and Astrophysics,*

*University of Würzburg, Am Hubland 97074 Würzburg, Germany*

<sup>4</sup>*Institute of Physics, Czech Academy of Sciences, Na Slovance 2, 182 21 Praha 8, Czechia*

We present a dynamical mean-field study of dynamical susceptibilities in two-band Hubbard model. Varying the model parameters we analyze the two-particle excitations in the normal as well as in the ordered phase, an excitonic condensate. The two-particle DMFT spectra in the ordered phase reveal the gapless Goldstone modes arising from spontaneous breaking of continuous symmetries. We also observe gapped Higgs mode, characterized by vanishing of the gap at the phase boundary. Qualitative changes observed in the spin susceptibility can be used as an experimental probe to identify the excitonic condensation.

Spontaneous symmetry breaking is a prominent demonstration of collective behavior in condensed matter systems. When continuous symmetry is broken in a system with short range interactions, the theory predicts appearance of gapless Goldstone excitations [4] and, under certain conditions [2], also gapped Higgs excitations. In particular, the latter ones have been subject of recent interest [2–5]. Description of collective excitations in interacting electron systems typically relies on perturbative approaches such as the random phase approximation in the weak-coupling limit [6, 7] or low-energy effective models in the strong-coupling limit [8, 9]. The dynamical mean-field theory (DMFT) [10, 11] uses a different approximation, the irreducible one-particle (1P) and two-particle (2P) vertices are assumed to be local. This simplification makes DMFT tractable for multi-orbital models with material realism [12, 13]. While DMFT has been widely used to study 1P dynamics, calculations of experimentally more relevant 2P susceptibilities for multi-orbital models are rare [3, 14–16, 18] and their behavior in broken-symmetry phase is unexplored.

In this Letter we use DMFT to study the dynamical susceptibilities in two-band Hubbard model across the excitonic transition [8, 19, 20]. The model choice is motivated by the experimental study of temperature and pressure-driven transition in Heisenberg dimer system  $\text{TlCuCl}_3$  [5] as well as a proposal of soft excitonic mode in  $\text{LaCoO}_3$  [21] based on resonant inelastic x-ray scattering (RIXS). On the theoretical side, the simple normal ground state of the model allows an approximate analytic treatment. The Hamiltonian of our model reads

$$H = \sum_{ij,\sigma} (a_{i\sigma}^\dagger \ b_{i\sigma}^\dagger) \begin{pmatrix} t_{aa} & t_{ab} \\ t_{ab} & t_{bb} \end{pmatrix} \begin{pmatrix} a_{j\sigma} \\ b_{j\sigma} \end{pmatrix} + \frac{\Delta}{2} \sum_{i,\sigma} (n_{i\sigma}^a - n_{i\sigma}^b) + U \sum_{i,\alpha} n_{i\uparrow}^\alpha n_{i\downarrow}^\alpha + \sum_{i,\sigma\sigma'} (U' - J\delta_{\sigma\sigma'}) n_{i\sigma}^a n_{i\sigma'}^b, \quad (1)$$

where  $a_{i\sigma}^\dagger$  and  $b_{i\sigma}^\dagger$  are the fermionic operators that create an electron with the respective orbital flavor and

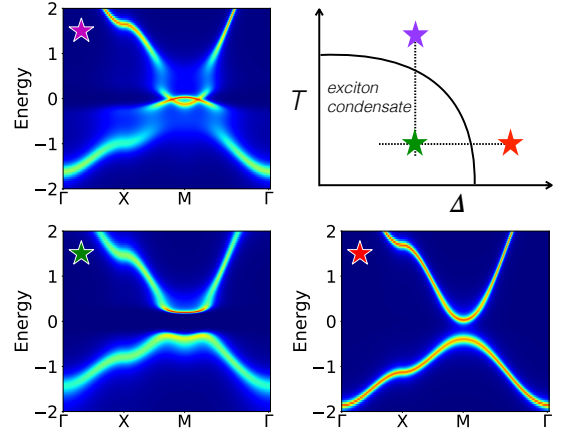


Figure 1. Sketch of the  $\Delta - T$  phase diagram with marked cuts, along which the susceptibilities are calculated. The 1P spectra at the points 3.55, 1/11 (violet), 3.55, 1/40 (green) and 3.8, 1/40 (blue).

spin  $\sigma$  at site  $i$  of a square lattice. The first term describes the nearest neighbor hopping. The remaining local terms, which can be written in terms of number operators  $n_{i,\sigma}^c \equiv c_{i\sigma}^\dagger c_{i\sigma}$ , capture the crystal-field splitting  $\Delta$ , the Hubbard interaction  $U$  and Hund’s exchange  $J$  in Ising approximation. Parameters  $U = 4$ ,  $J = 1$ ,  $U' = U - 2J$ ,  $t_{aa} = 0.4118$ ,  $t_{bb} = -0.1882$ ,  $t_{ab} = 0$  (0.02) were used in previous studies of the model [3, 22, 23].

Our calculations follow the standard DMFT procedure of mapping the lattice model onto an auxiliary Anderson impurity model (AIM) [24, 25], which is used to determine the local one-particle (1P) and two-particle (2P) irreducible vertices. The auxiliary AIM is solved using the continuous-time quantum Monte-Carlo (CT-QMC) algorithm in the hybridization expansion formalism [26] in the open source implementation provided by the ALP-SCore collaboration [27–29]. Numerically identical results for normal state susceptibilities were obtained with w2dynamics [30].

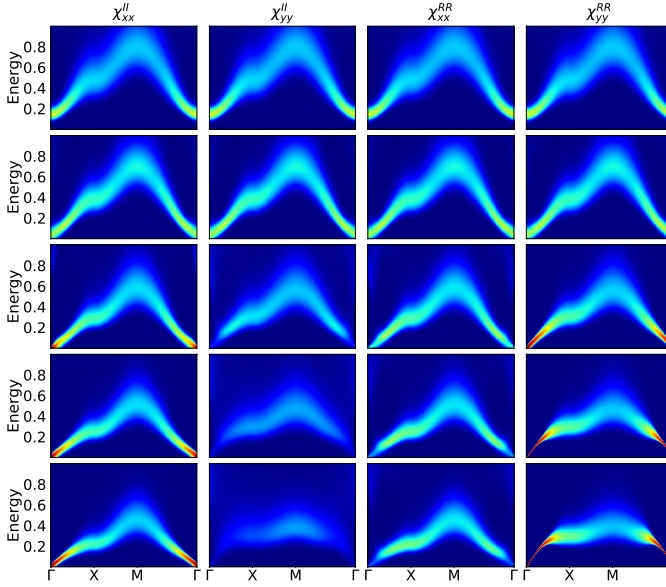


Figure 2. Evolution of the excitonic modes of the dynamical susceptibility across the low-temperature ( $T = 1/40$ ) 'quantum' phase transition driven by  $\Delta$  in the  $U^2(1)$  model ( $t_{ab}=0$ ). The columns correspond to the susceptibilities  $\chi_{\gamma\gamma}^{OO}$  with  $O^\gamma = I^x, I^y, R^x, R^y$  (left to right) along the high-symmetry lines in the 2D Brillouin zone. The rows from top to bottom correspond to  $\Delta = 3.9, 3.8, 3.65, 3.55, 3.45$  with  $\Delta_c \approx 3.75$ . The order parameter has the form  $\phi = (0, i)|\phi|$ . Complete results for all studied values of  $\Delta$  can be found in SM [32].

The 2P dynamics of the system is described by susceptibilities  $\chi_{\eta\eta}^{OO}(\mathbf{k}, \omega)$ , which we obtain by analytic continuation [31, 32] from the imaginary Matsubara frequencies

$$\chi_{\eta\eta}^{OO}(\mathbf{k}, i\nu_n) = \sum_{\mathbf{R}} \int_0^\beta d\tau e^{i(\nu_n\tau + \mathbf{k}\cdot\mathbf{R})} \langle O_{\mathbf{i}+\mathbf{R}}^\eta(\tau) O_{\mathbf{i}}^\eta(0) \rangle - \langle O^\eta \rangle^2$$

The observables of interest  $O^\eta$  in the following will be the excitonic operators  $R_i^\eta = \sigma_{\alpha\beta}^\eta a_{i\alpha}^\dagger b_{i\beta} + (\sigma_{\alpha\beta}^\eta)^* a_{i\alpha}^\dagger b_{i\beta}$ ,  $I_i^\eta = i\sigma_{\alpha\beta}^\eta a_{i\alpha}^\dagger b_{i\beta} - i(\sigma_{\alpha\beta}^\eta)^* a_{i\alpha}^\dagger b_{i\beta}$  with  $\eta = x, y$  and the  $z$ -component of spin  $S_i^z = \sigma_{\alpha\beta}^z (a_{i\alpha}^\dagger a_{i\beta} + b_{i\alpha}^\dagger b_{i\beta})$ , where  $\sigma^\eta$  are the standard Pauli matrices. [10]

Susceptibility  $\chi_{\eta\eta}^{OO}(\mathbf{k}, i\nu_n)$  is obtained from the general particle-hole susceptibility  $[\bar{\chi}]_{\alpha\beta, \gamma\delta}(\mathbf{k}, i\nu_n)$ , the primary computed quantity indexed by pairs of fermionic flavors ( $\alpha, \dots, \delta = a \uparrow, a \downarrow, b \uparrow, b \downarrow$ ). In the normal state, the  $16 \times 16$  matrix  $\bar{\chi}(\mathbf{k}, i\nu_n)$  can be block diagonalized into the charge, spin longitudinal, spin transverse channels in the standard way. In the ordered state, however,  $\bar{\chi}(\mathbf{k}, i\nu_n)$  becomes dense. Numerically,  $\bar{\chi}(\mathbf{k}, i\nu_n)$  is obtained by repeated solution of Bethe-Salpeter equation for each  $(\mathbf{k}, i\nu_n)$  [14] using the orthogonal polynomial representation [34].

In general, model (1) has a rich physics [3, 18, 35–37]. At half-filling and present parameters it undergoes a second-order phase transition to polar exciton conden-

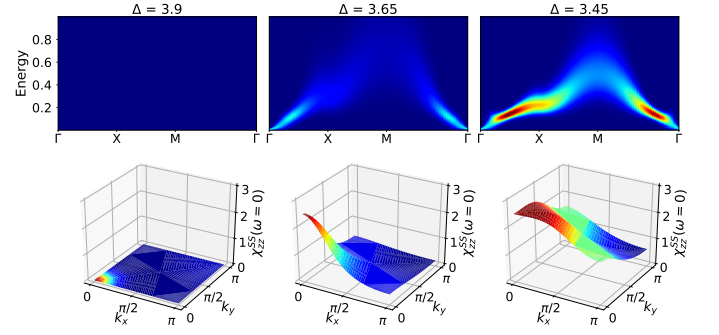


Figure 3. (a) Evolution of dynamical spin susceptibility  $\chi_{zz}^{SS}(\mathbf{k}, \omega)$  across the phase transition driven by  $\Delta$  as in Fig. 2. (b) The corresponding static susceptibilities  $\chi_{zz}^{SS}(\mathbf{k}, 0)$  throughout the Brillouin zone.

sate (PEC), which can be driven by temperature or the crystal field  $\Delta$  [3], as indicated in Fig. 1a. The exciton condensation can be detected by a 2D-complex-vector order parameter  $\phi^\eta = \sigma_{\alpha\beta}^\eta \langle a_{i\alpha}^\dagger b_{i\beta} \rangle$ . [11] The order parameter  $\phi$  in the PEC phase has the form  $\phi = e^{i\varphi} \mathbf{v}$ , where  $\mathbf{v}$  has an arbitrary direction in the  $xy$ -plane that is fixed at the transition. Presence or absence of the cross-hopping  $t_{ab}$  affects the symmetry of (1) as well as the type of symmetry breaking. For  $t_{ab} = 0$ ,  $U(1) \times U(1)$  symmetry, corresponding to the  $z$ -axis spin rotation (relative  $\uparrow - \downarrow$  gauge symmetry) times the relative  $a - b$  gauge symmetry, is broken and  $\varphi$  freezes at an arbitrary value at the transition. We will refer to this case as the  $U^2(1)$  model. For  $t_{ab} \neq 0$ , the relative  $a - b$  phase is fixed by the cross-hopping term. Only the  $U(1)$  spin rotation symmetry is broken at the transition, while the phase  $e^{i\varphi}$  is purely imaginary. [23] We will refer to this case as the  $U(1)$  model. In all calculations we choose the orientation  $\phi \sim (0, i)$  and the results will be reported relative to it.

First, we discuss the  $U^2(1)$  case and the 'quantum' [13] phase transition driven by crystal field  $\Delta$ . While the system remains an insulator with a sizable 1P gap throughout the studied  $\Delta$ -range, Fig. 1, the 2P spectrum contains low-energy excitations. In the normal phase ( $\Delta > \Delta_c$ ), these can be viewed as spinful Frenkel excitons, which give rise to sharp dispersive features in the (identical) excitonic susceptibilities shown in Fig. 2.

Reducing  $\Delta$  causes the excitation gap to close and the system undergoes a transition to the PEC phase. The degeneracy of the susceptibilities in Fig. 2 is lifted. The  $\chi_{yy}^{RR}$  and  $\chi_{xx}^{II}$  show gapless and linear dispersions with intensities diverging as  $1/|\mathbf{k}|$  (see SM [32]). These correspond to two linear Goldstone modes predicted by general theory [4] for the case of two broken symmetry generators with a vanishing commutator. Besides the different sound velocities 4a for the two modes, there is a pronounced difference between  $\chi_{yy}^{II}$  and  $\chi_{yy}^{RR}$ , while  $\chi_{xx}^{II}$  and  $\chi_{xx}^{RR}$  are more similar to each other. We show below that this behavior is related to a point of accidentally

enhanced symmetry.

The spin susceptibility  $\chi_{zz}^{SS}$  in Fig. 3 undergoes a striking change at the phase transition. In the normal phase,  $\chi_{zz}^{SS}$  has a tiny amplitude and no distinct dispersive features as may be expected of a band insulator. In the PEC phase, it develops a sharp low-energy dispersion although there are no ordered moments present. The shape of the dispersive feature strongly resembles  $\chi_{xx}^{RR}$ .

Turning on a small cross-hopping  $t_{ab} = 0.02$  leads to a generic  $U(1)$  model. The overall shapes of the susceptibilities remain unchanged, but the details change as shown in Fig. 5. As in the  $U^2(1)$  case the phase transition proceeds by closing of the exciton gap. While  $\chi_{xx}^{II}$ , detecting the Goldstone spin-rotation mode in our setup, remains gapless and linear in the PEC phase,  $\chi_{yy}^{RR}$  exhibits a gap that increases when moving away from the phase boundary, see Fig. 4b. Such a behavior characteristic of Higgs mode was observed in bi-layer Heisenberg system  $\text{TiCuCl}_3$  [5]. We point out that bi-layer Heisenberg model is closely related to (7) [40]. The behavior of the spin susceptibility  $\chi_{zz}^{SS}$  and its relationship to  $\chi_{xx}^{RR}$  is essentially the same as in the  $U^2(1)$  case.

To understand the present numerical data, it is instructive to analyze the strong-coupling coupling limit of (1), which allows analytical treatment. The model can be written in terms of two-flavor hard-core bosons [2, 40, 41]

$$\mathcal{H} = \mu \sum_i n_i - \sum_{ij,\nu} \left[ \mathcal{T} d_{i\nu}^\dagger d_{j\nu} - \frac{\mathcal{W}}{2} (d_{i\nu}^\dagger d_{j\nu}^\dagger + d_{i\nu} d_{j\nu}) \right] + \frac{\mathcal{V}}{2} \sum_{ij} n_i n_j + \frac{\mathcal{J}}{2} \sum_{ij} S_i^z S_j^z, \quad (2)$$

Here,  $d_{i\nu}^\dagger$  ( $\nu = x, y$ ) are bosonic operators obtained by 'gluing' two fermionic operators  $\frac{1}{\sqrt{2}} \sigma_{\alpha\beta}^\nu a_{i\alpha}^\dagger b_{i\beta} \rightarrow d_{i\nu}^\dagger$  together [3]. Acting on the low-spin (LS) state  $d_{i\nu}^\dagger$  create high-spin (HS) states. The number operators

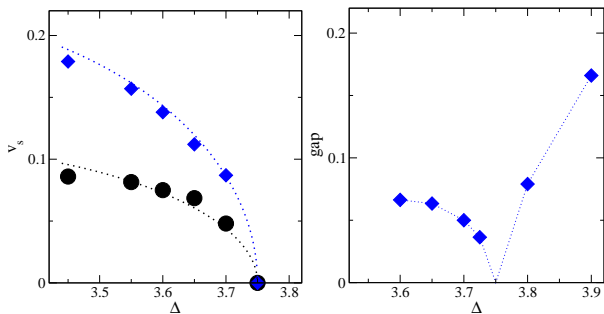


Figure 4. (a) The sound velocity of the Goldstone modes, the phase mode ( $\chi_{yy}^{RR}$ , blue symbols) and the spin rotation mode ( $\chi_x^{II}$ , black symbols) in the  $U^2(1)$  model as a function of the crystal field  $\Delta$ . The dotted lines show the corresponding strong-coupling results. (b) The Higgs gap in the  $U(1)$  model with  $t_{ab} = 0.02$  as a function of  $\Delta$ . The line is a guide for eyes.

Table I. The parameters of Eq. 3. The variational parameter  $0 \leq \alpha^2 \leq 1$ , corresponding to the LS density, assumes 1 in the normal phase and  $\frac{\mu+z(\mathcal{T}+\mathcal{W})+z\mathcal{V}}{2z(\mathcal{T}+\mathcal{W})+z\mathcal{V}}$  in the condensate.

$\mu_x$	$\alpha^2 \mu + z \alpha^2 (1 - \alpha^2) (2\mathcal{T} + 2\mathcal{W} + \mathcal{V})$
$\mathcal{T}_x$	$\alpha^2 \mathcal{T} - (1 - \alpha^2) \mathcal{J}$
$\mathcal{W}_x$	$\alpha^2 \mathcal{W} + (1 - \alpha^2) \mathcal{J}$
$\mu_y$	$z(\mathcal{T} + \mathcal{W}); \mu$ if $\alpha^2 = 1$
$\mathcal{T}_y$	$\mathcal{T} - \alpha^2 (1 - \alpha^2) (2\mathcal{T} + 2\mathcal{W} + \mathcal{V})$
$\mathcal{W}_y$	$\mathcal{W} - \alpha^2 (1 - \alpha^2) (2\mathcal{T} - 2\mathcal{W} + \mathcal{V})$

$n_i = \sum_\nu d_{i\nu}^\dagger d_{i\nu}$  measure the HS concentration and  $S_i^z = -i(d_{ix}^\dagger d_{iy} - d_{iy}^\dagger d_{ix})$  is  $z$ -component of the spin operator. The propagators of the  $d$ -bosons are related to the excitonic susceptibilities by the map  $R^\nu \rightarrow d_\nu^\dagger + d_\nu$ ,  $I^\nu \rightarrow id_\nu^\dagger - id_\nu$ . Since  $\mathcal{W} \sim t_{ab}^2$ , the relative  $a$ - $b$  gauge freedom of the  $U^2(1)$  version of model (1) translates to the conservation of the number of  $d$ -bosons ( $\mathcal{W} = 0$ ) in (7).

Generalized spin wave treatment [1, 2] of (7), see SM [32] for details, leads to a free boson model

$$\tilde{\mathcal{H}}_\nu = \mu_\nu \sum_i \tilde{n}_{i\nu} - \sum_{ij} \left[ \mathcal{T}_\nu \tilde{d}_{i\nu}^\dagger \tilde{d}_{j\nu} - \frac{\mathcal{W}_\nu}{2} (\tilde{d}_{i\nu}^\dagger \tilde{d}_{j\nu}^\dagger + H.c.) \right]. \quad (3)$$

Note that the parameters of this effective model given in Table II depend (in the ordered phase) on the flavor  $\nu = x, y$ . Similar to DMFT, the approximation leading to (3) is insensitive to the dimensionality and is justified only in higher dimensions. The elementary excitations of (3) have the dispersion  $\epsilon_\nu(\mathbf{k}) = \sqrt{(\mu_\nu - 2\mathcal{T}_\nu \delta(\mathbf{k}))^2 - (2\mathcal{W}_\nu \delta(\mathbf{k}))^2}$  with  $\delta(\mathbf{k}) = \cos k_x + \cos k_y$ . For the  $U^2(1)$  case with  $\mathcal{W} = 0$  both  $x$  and

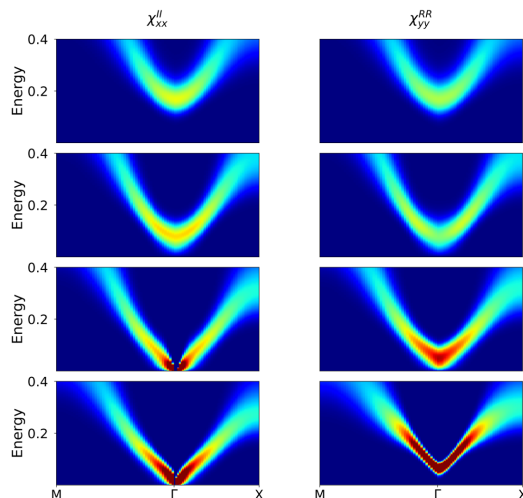


Figure 5. The  $\chi_{xx}^{II}$  and  $\chi_{yy}^{RR}$  in the vicinity of  $\Gamma$ -point for  $U(1)$  model with small finite cross-hopping  $t_{ab} = 0.02$ . The rows from top to bottom correspond to  $\Delta = 3.90, 3.80, 3.7, 3.6$  with  $\Delta_c \approx 3.75$ . The order parameter has the form  $\phi = (0, i)|\phi\rangle$ . The overall shape of the susceptibilities (see SM [32]) is the same as in Fig. 2.

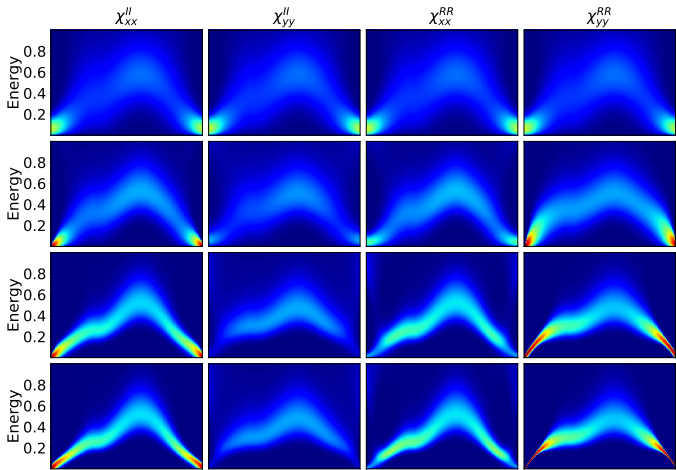


Figure 6. The same susceptibilities as in Fig. 2 calculated across the thermally driven transition for  $\Delta = 3.55$ . The rows from top to bottom correspond to inverse temperatures  $\beta = 11, 16, 30, 40$  with  $\beta_c \approx 13$ .

$y$  modes are gapless. The corresponding sound velocities  $v_\nu \equiv \nabla_{\mathbf{k}} \epsilon_\nu(\mathbf{k}) = \sqrt{8|\mathcal{W}_\nu|(\mathcal{T}_\nu + |\mathcal{W}_\nu|)}$ , increase as  $|\mu - \mu_c|^{1/2}$  in the ordered phase, compare to Fig. 4a, while the ratio  $v_x/v_y \sim \mathcal{J}^{1/2}$  is independent of  $\mu$ . [32]

The sound velocity  $v_x$  vanishes completely for  $\mathcal{J} = 0$  and the  $\tilde{d}_x$ -mode becomes gapless quadratic. The symmetry of (7) at this point is enhanced to  $U(2)$  with four generators. In the condensate three out of its four generators are broken, however, there is one commutator with finite expectation value. According to Ref. 4 this implies one linear and one quadratic Goldstone mode. In the phase diagram of (7)  $\mathcal{J} = 0$  lies at the boundary between the polar and ferromagnetic exciton (FMEC) condensates. The smallness of calculated  $v_x/v_y$  as well as the similarity of  $\chi_{xx}^{RR}$  and  $\chi_{xx}^{II}$  show that the effective  $\mathcal{J}$  is small and the condensate (but not the normal state) is close to a ferromagnetic instability [6, 44]. Indeed, previous studies [22] showed that a small doping can bring the system to the FMEC state.

How is this behavior related to the spin susceptibility  $\chi_{zz}^{SS}$  in Fig. 3? Replacing the operator  $d_{iy}$  in the strong-coupling expression for  $S_i^z$  by its finite ordered value yields  $S_i^z \sim (d_{ix}^\dagger + d_{ix})|\phi\rangle$ . In the ordered phase, the spin susceptibility  $\chi_{zz}^{SS}$  therefore follows  $\chi_{xx}^{RR}$ , while they are decoupled in the normal phase. As  $\mathcal{J} \rightarrow 0^+$ , the dispersive feature in  $\chi_{xx}^{RR}$  and  $\chi_{zz}^{SS}$  approaches the point  $(\mathbf{k}, \omega) = (0, 0)$  marking the ferromagnetic instability. [45] This does not happen by shift of the feature, but growing spectral weight at low  $\mathbf{k}$ .

Turning the finite  $\mathcal{T}$  in (7) on, removes the  $U(1)$  symmetry associated with conservation of  $d$ -bosons. The  $d_x$  mode remains gapless, while the  $d_y$  mode acquires a gap that vanishes only at the transition [32] in the fashion observed in the DMFT data.

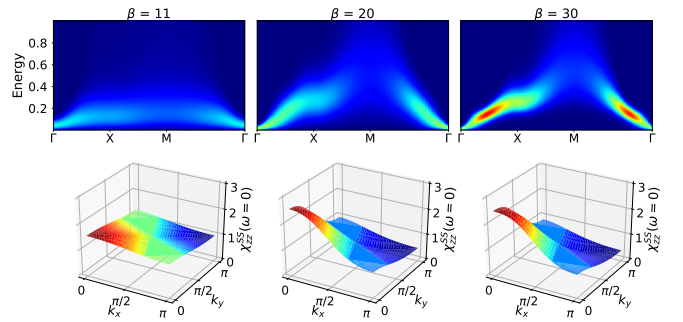


Figure 7. (a) Evolution of dynamical spin susceptibility  $\chi_{zz}^{SS}(\mathbf{k}, \omega)$  across the thermally driven phase transition as in Fig. 6 for inverse temperatures  $\beta = 11, 20, 30$  (left to right). (b) The corresponding static susceptibilities  $\chi_{zz}^{SS}(\mathbf{k}, 0)$  throughout the Brillouin zone.

Finally, we investigate the thermally driven transition in the  $U^2(1)$  model indicated by the vertical line in Fig. 1. The evolution of the excitonic and susceptibilities is shown in Fig. 6. The main observation is that, similar to the ‘quantum’ case driven by  $\Delta$ , the phase transition can be viewed as a mode softening, an observation also made in  $\text{TlCuCl}_3$  [5]. At the transition, the gap in the ‘Goldstone susceptibilities’  $\chi_{yy}^{RR}$  and  $\chi_{xx}^{II}$  disappears, while a small but finite gap survives in the complementary elements  $\chi_{xx}^{RR}$  and  $\chi_{yy}^{II}$ . On cooling the system deeper into the ordered phase the low- $|\mathbf{k}|$  spectral weight of the latter susceptibilities diminishes.

Unlike in the low- $T$ -high- $\Delta$  corner of the phase diagram in Fig. 1a, the normal state spin susceptibility  $\chi_{zz}^{SS}$  in Fig. 7 has non-negligible amplitude and some structure at low-energies. This is due to the presence of thermally excited HS states and possibly 1P excitations. Nevertheless, also in this case  $\chi_{zz}^{SS}$  changes qualitatively at the transition. The dispersion becomes sharper, significantly broader and with enhanced amplitude at small  $\mathbf{k}$ , except for the close vicinity of  $\mathbf{k} = 0$ . The similarity between  $\chi_{zz}^{SS}$  and  $\chi_{xx}^{RR}$ , discussed above, quickly builds up upon entering the excitonic phase.

We close the presentation by a few technical remarks. The calculations were performed with a matrix version of the QMC code, which can be applied directly to problems with spin  $SU(2)$  symmetry. We have chosen the Ising-like model (1) for the following reasons: i) its phase diagram is known from previous studies [3, 22, 23], ii) while involving breaking of continuous symmetries, its  $U(1) \times U(1)$  symmetry is somewhat simpler than  $U(1) \times SU(2)$  of its fully rotationally invariant analog and thus a natural choice for initial study, iii) the excitonic transition in  $SU(2)$  symmetric model happens at lower temperatures [46] and thus is more numerically demanding to study.

In conclusion, we used DMFT to study the 2P response across exciton condensation transition in two-orbital Hubbard model, an example of a second-order

phase transition that breaks a continuous symmetry. We observed formation of Goldstone modes predicted by general theory [4], as well as appearance of a Higgs mode [2], characterized by vanishing of the gap at the phase transitions. Our results in general agree with the experimental observations on  $\text{TlCuCl}_3$  [5]. We showed how the dynamical susceptibility reflects accidental symmetries, e.g., at a phase boundary, as is the case of PEC/FMEC transition in the studied model. Finally, we showed that the formation of polar exciton condensate has a profound effect on the dynamical spin susceptibility, which can be used as an experimentally observable signature of this exotic state.

We thank J. Chaloupka, G. Sangiovanni, G. Khaliullin and B. Hartl for discussions, H. Shinaoka for help with the ALPS code, K. Steiner and O. Janson for testing the maximum entropy code, and K. Held and A. Kauch for critical reading of the manuscript. This work was supported by the ERC Grant Agreements No. 646807 under EU Horizon 2020 (J.Ku., A.Har. and D.G.) and No. 306447 under EU Seventh Framework Program (FP7/20072013)/ERC (J.Ka.), by the Czech Ministry of Education, Youth and Sports, project “IT4Innovations National Supercomputing Center – LM2015070” and by project MUNI/A/1310/2016 (D.G.), by FWF through SFB ViCoM F41 (J.Ka.), by DFG through SFB1170 “Tocotronics” (A.Hau.) and by the Austrian Federal Ministry of Science, Research and Economy through the Vienna Scientific Cluster (VSC) Research Center (P.G.). We gratefully acknowledge the Gauss Centre for Supercomputing e.V. ([www.gauss-centre.eu](http://www.gauss-centre.eu)) for providing computing time on the GCS Supercomputer SuperMUC at Leibniz Supercomputing Centre ([www.lrz.de](http://www.lrz.de)), the programme “Projects of Large Research, Development, and Innovations Infrastructures” (CESNET LM2015042) for the access to computing and storage facilities of the Czech National Grid Infrastructure MetaCentrum, and the Vienna Scientific Cluster (VSC) for access to its computing facilities.

---

[4] H. Watanabe and H. Murayama, *Phys. Rev. Lett.* **108**, 251602 (2012).  
 [2] D. Pekker and C. Varma, *Annual Review of Condensed Matter Physics* **6**, 269 (2015).  
 [3] A. Jain, M. Krautloher, J. Porras, G. H. Ryu, D. P. Chen, D. L. Abernathy, J. T. Park, A. Ivanov, J. Chaloupka, G. Khaliullin, B. Keimer, and B. J. Kim, *Nat. Phys.* **13**, 633 (2017).  
 [4] D. Sherman, U. S. Pracht, B. Gorshunov, S. Poran, J. Jesudasan, M. Chand, P. Raychaudhuri, M. Swanson, N. Trivedi, A. Auerbach, M. Scheffler, A. Frydman, and M. Dressel, *Nature Physics* **11**, 188 EP (2015), article.  
 [5] P. Merchant, B. Normand, K. W. Krämer, M. Boehm, D. F. McMorrow, and C. Rüegg, *Nature Physics* **10**, 373 (2014).

[6] E. Bascones, A. A. Burkov, and A. H. MacDonald, *Phys. Rev. Lett.* **89**, 086401 (2002).  
 [7] T. Yamaguchi, K. Sugimoto, and Y. Ohta, *J. Phys. Soc. Japan* **86**, 043701 (2017).  
 [8] G. Khaliullin, *Phys. Rev. Lett.* **111**, 197201 (2013).  
 [9] T. Tatsumo, E. Mizoguchi, J. Nasu, M. Naka, and S. Ishihara, *J. Phys. Soc. Japan* **85**, 83706 (2016).  
 [10] W. Metzner and D. Vollhardt, *Phys. Rev. Lett.* **62**, 324 (1989).  
 [11] A. Georges, G. Kotliar, W. Krauth, and M. Rozenberg, *Rev. Mod. Phys.* **68**, 13 (1996).  
 [12] G. Kotliar, S. Y. Savrasov, K. Haule, V. S. Oudovenko, O. Parcollet, and C. A. Marianetti, *Rev. Mod. Phys.* **78**, 865 (2006).  
 [13] K. Held, *Advances in Physics* **56**, 829 (2007).  
 [14] J. Kuneš, *Phys. Rev. B* **83**, 085102 (2011).  
 [15] H. Park, K. Haule, and G. Kotliar, *Phys. Rev. Lett.* **107**, 137007 (2011).  
 [16] L. Boehnke and F. Lechermann, *physica status solidi (a)* **211**, 1267 (2013).  
 [3] J. Kuneš and P. Augustinský, *Phys. Rev. B* **89**, 115134 (2014).  
 [18] S. Hoshino and P. Werner, *Phys. Rev. B* **93**, 155161 (2016).  
 [19] N. F. Mott, *Philos. Mag.* **6**, 287 (1961).  
 [20] B. I. Halperin and T. M. Rice, “Solid state physics,” (Academic Press, New York, 1968) p. 115.  
 [21] R.-P. Wang, A. Hariki, A. Sotnikov, F. Frati, J. Okamoto, H.-Y. Huang, A. Singh, D.-J. Huang, K. Tomiyasu, C.-H. Du, J. Kuneš, and F. M. F. de Groot, *Phys. Rev. B* **98**, 035149 (2018).  
 [22] J. Kuneš, *Phys. Rev. B* **90**, 235140 (2014).  
 [23] J. Kuneš and D. Geffroy, *Phys. Rev. Lett.* **116**, 256403 (2016).  
 [24] A. Georges and G. Kotliar, *Phys. Rev. B* **45**, 6479 (1992).  
 [25] M. Jarrell, *Phys. Rev. Lett.* **69**, 168 (1992).  
 [26] P. Werner, A. Comanac, L. de’ Medici, M. Troyer, and A. J. Millis, *Phys. Rev. Lett.* **97**, 076405 (2006).  
 [27] B. Bauer, L. D. Carr, H. G. Evertz, A. Feiguin, J. Freire, S. Fuchs, L. Gamper, J. Gukelberger, E. Gull, S. Guertler, A. Hehn, R. Igarashi, S. V. Isakov, D. Koop, P. N. Ma, P. Mates, H. Matsuo, O. Parcollet, G. Pawłowski, J. D. Picon, L. Pollet, E. Santos, V. W. Scarola, U. Schollwöck, C. Silva, B. Surer, S. Todo, S. Trebst, M. Troyer, M. L. Wall, P. Werner, and S. Wessel, *J. Stat. Mech. Theory Exp.* **2011**, P05001 (2011).  
 [28] H. Shinaoka, E. Gull, and P. Werner, *Comput. Phys. Commun.* **215**, 128 (2017).  
 [29] A. Gaenko, A. E. Antipov, G. Carcassi, T. Chen, X. Chen, Q. Dong, L. Gamper, J. Gukelberger, R. Igarashi, S. Isakov, M. Könz, J. P. LeBlanc, R. Levy, P. N. Ma, J. E. Paki, H. Shinaoka, S. Todo, M. Troyer, and E. Gull, *Comput. Phys. Commun.* **213**, 235 (2017).  
 [30] M. Wallerberger, A. Hausoel, P. Gunacker, A. Kowalski, N. Parragh, F. Goth, K. Held, and G. Sangiovanni, *ArXiv:1801.10209*.  
 [31] J. E. Gubernatis, M. Jarrell, R. N. Silver, and D. S. Sivia, *Phys. Rev. B* **44**, 6011 (1991).  
 [32] Supplemental Material.  
 [10] The barred indices imply summation.  
 [34] *Phys. Rev. B* **84**, 1 (2011).  
 [35] P. Werner and A. J. Millis, *Phys. Rev. Lett.* **99**, 126405 (2007).  
 [36] T. Kaneko and Y. Ohta, *Phys. Rev. B* **90**, 245144 (2014).

- [37] T. Kaneko, B. Zenker, H. Fehske, and Y. Ohta, *Phys. Rev. B* **92**, 115106 (2015).
- [11] For an interaction with full  $SU(2)$  spin-rotational symmetry  $\phi$  is a 3D vector.
- [13] We expect no substantial difference between on the present and  $T = 0$  within DMFT approximation.
- [40] J. Kuneš, *J. Phys. Condens. Matter* **27**, 333201 (2015).
- [41] L. Balents, *Phys. Rev. B* **62**, 2346 (2000).
- [2] J. Nasu, T. Watanabe, M. Naka, and S. Ishihara, *Phys. Rev. B* **93**, 205136 (2016).
- [1] T. Sommer, M. Vojta, and K. Becker, *Eur. Phys. J. B* **23**, 329 (2001).
- [44] B. A. Volkov and Y. V. Kopaev, *JETP Lett.* **19**, 104 (1973).
- [45] The present analysis cannot be used if  $\mathcal{J} < 0$  since the FMEC phase corresponds to a different ground state.
- [46] D. Geffroy, A. Hariki, and J. Kuneš, *Phys. Rev. B* **97**, 155114 (2018).

## Supplementary Material

### Generalized spin-wave treatment for two flavor bosons

In the following we reproduce the generalized spin-wave treatment of Ref. 1 in the notation of the present paper. As far as we understand the results are identical to the generalized Primakoff-Holstein approach [2]. We study Hamiltonian in Schwinger boson representation

$$\begin{aligned}
H = & \mu \sum_{\mathbf{i}, \alpha} b_{\mathbf{i}, \alpha}^\dagger b_{\mathbf{i}, \alpha} - t \sum_{\mathbf{i}, \alpha} \sum_{\boldsymbol{\delta}} b_{\mathbf{i}+\boldsymbol{\delta}, \alpha}^\dagger s_{\mathbf{i}+\boldsymbol{\delta}} s_{\mathbf{i}}^\dagger b_{\mathbf{i}, \alpha} + \sum_{\mathbf{i}, \alpha, \beta} \sum_{\boldsymbol{\delta}} \left( \frac{V}{2} + \frac{J}{2} \alpha \beta \right) b_{\mathbf{i}, \alpha}^\dagger b_{\mathbf{i}+\boldsymbol{\delta}, \beta}^\dagger b_{\mathbf{i}, \alpha} b_{\mathbf{i}+\boldsymbol{\delta}, \beta} \\
& + \frac{W}{2} \sum_{\mathbf{i}, \alpha} \sum_{\boldsymbol{\delta}} \left( b_{\mathbf{i}+\boldsymbol{\delta}, \alpha}^\dagger s_{\mathbf{i}+\boldsymbol{\delta}} b_{\mathbf{i}, -\alpha}^\dagger s_{\mathbf{i}} + s_{\mathbf{i}+\boldsymbol{\delta}}^\dagger b_{\mathbf{i}+\boldsymbol{\delta}, \alpha} s_{\mathbf{i}}^\dagger b_{\mathbf{i}, -\alpha} \right),
\end{aligned} \tag{4}$$

where  $\alpha = \pm 1$  and  $\boldsymbol{\delta} = (0, 1), (1, 0), (0, -1), (-1, 0)$ . The  $b$  and  $s$  operators have bosonic commutation relations and the physical states fulfill the constraint  $b_{\mathbf{i}, 1}^\dagger b_{\mathbf{i}, 1} + b_{\mathbf{i}, -1}^\dagger b_{\mathbf{i}, -1} + s_{\mathbf{i}}^\dagger s_{\mathbf{i}} = 1$  on each lattice site  $\mathbf{i}$ . Anticipating the polar condensate we go to the Cartesian basis

$$b_1^\dagger = \frac{1}{\sqrt{2}}(b_x^\dagger + ib_y^\dagger) \quad b_{-1}^\dagger = \frac{1}{\sqrt{2}}(b_x^\dagger - ib_y^\dagger), \tag{5}$$

where

$$S^z = b_1^\dagger b_1 - b_{-1}^\dagger b_{-1} = -i(b_x^\dagger b_y - b_y^\dagger b_x). \tag{6}$$

In the Cartesian basis

$$\begin{aligned}
H = & \mu \sum_{\mathbf{i}} b_{\mathbf{i}, x}^\dagger b_{\mathbf{i}, x} - t \sum_{\mathbf{i}} \sum_{\boldsymbol{\delta}} b_{\mathbf{i}+\boldsymbol{\delta}, x}^\dagger s_{\mathbf{i}+\boldsymbol{\delta}} s_{\mathbf{i}}^\dagger b_{\mathbf{i}, x} + \mu \sum_{\mathbf{i}} b_{\mathbf{i}, y}^\dagger b_{\mathbf{i}, y} - t \sum_{\mathbf{i}} \sum_{\boldsymbol{\delta}} b_{\mathbf{i}+\boldsymbol{\delta}, y}^\dagger s_{\mathbf{i}+\boldsymbol{\delta}} s_{\mathbf{i}}^\dagger b_{\mathbf{i}, y} \\
& + \frac{V}{2} \sum_{\mathbf{i}} \sum_{\boldsymbol{\delta}} \left( b_{\mathbf{i}, x}^\dagger b_{\mathbf{i}, x} + b_{\mathbf{i}, y}^\dagger b_{\mathbf{i}, y} \right) \left( b_{\mathbf{i}+\boldsymbol{\delta}, x}^\dagger b_{\mathbf{i}+\boldsymbol{\delta}, x} + b_{\mathbf{i}+\boldsymbol{\delta}, y}^\dagger b_{\mathbf{i}+\boldsymbol{\delta}, y} \right) \\
& - \frac{J}{2} \sum_{\mathbf{i}} \sum_{\boldsymbol{\delta}} \left( b_{\mathbf{i}, x}^\dagger b_{\mathbf{i}, y} - b_{\mathbf{i}, y}^\dagger b_{\mathbf{i}, x} \right) \left( b_{\mathbf{i}+\boldsymbol{\delta}, x}^\dagger b_{\mathbf{i}+\boldsymbol{\delta}, y} - b_{\mathbf{i}+\boldsymbol{\delta}, y}^\dagger b_{\mathbf{i}+\boldsymbol{\delta}, x} \right) \\
& + \frac{W}{2} \sum_{\mathbf{i}} \sum_{\boldsymbol{\delta}} \left( b_{\mathbf{i}+\boldsymbol{\delta}, x}^\dagger s_{\mathbf{i}+\boldsymbol{\delta}} b_{\mathbf{i}, x}^\dagger s_{\mathbf{i}} + b_{\mathbf{i}+\boldsymbol{\delta}, y}^\dagger s_{\mathbf{i}+\boldsymbol{\delta}} b_{\mathbf{i}, y}^\dagger s_{\mathbf{i}} + s_{\mathbf{i}+\boldsymbol{\delta}}^\dagger b_{\mathbf{i}+\boldsymbol{\delta}, x} s_{\mathbf{i}}^\dagger b_{\mathbf{i}, x} + s_{\mathbf{i}+\boldsymbol{\delta}}^\dagger b_{\mathbf{i}+\boldsymbol{\delta}, y} s_{\mathbf{i}}^\dagger b_{\mathbf{i}, y} \right).
\end{aligned} \tag{7}$$

Next, we search for a variational ground state of the form

$$|G\rangle = \prod_{\mathbf{i}} (\alpha s_{\mathbf{i}}^\dagger + \beta b_{\mathbf{i}, y}^\dagger + \gamma b_{\mathbf{i}, x}^\dagger) |\emptyset\rangle, \quad |\alpha|^2 + |\beta|^2 + |\gamma|^2 = 1. \tag{8}$$

This is a reasonable ansatz for sufficiently large  $t > 0$ . The energy density per lattice site in  $|G\rangle$  is given by

$$\begin{aligned}
\frac{1}{N} \langle G | \tilde{H} | G \rangle = & \mu (|\beta|^2 + |\gamma|^2) - zt (|\alpha|^2 |\beta|^2 + |\alpha|^2 |\gamma|^2) + \frac{zV}{2} (|\beta|^2 + |\gamma|^2)^2 \\
& - \frac{zJ}{2} (\gamma^* \beta - \beta^* \gamma)^2 + \frac{zW}{2} \alpha^2 (\beta^2 + \gamma^2 + (\beta^*)^2 + (\gamma^*)^2).
\end{aligned} \tag{9}$$

With  $J > 0$  we get that  $\text{Im}(\gamma^* \beta) = 0$ , which we choose to satisfy by  $\gamma = 0$ . Without loss of generality we set  $\alpha$  to be real and positive. With  $W = 0$  is the phase of  $\beta$  arbitrary, while for finite  $W$  we get the minimum for imaginary  $\beta$  if  $W > 0$  and for real  $\beta$  if  $W < 0$ , i.e.  $\beta^2 \propto -\text{sgn } W$ . In both cases we get

$$\frac{1}{N} \langle G | \tilde{H} | G \rangle = \mu(1 - \alpha^2) - z(t + |W|)\alpha^2(1 - \alpha^2) + \frac{zV}{2}(1 - \alpha^2)^2, \tag{10}$$

where we have used  $W(\beta^2 + (\beta^*)^2) = -2|W|(1 - \alpha^2)$ . Solving for  $\alpha$  we get

$$\alpha^2 = \frac{\mu + z(t + |W|) + zV}{2z(t + |W|) + zV} \tag{11}$$

Next, we perform a local transformation

$$s^\dagger = \alpha \tilde{s}^\dagger - \beta \tilde{b}_y^\dagger, \quad s = \alpha \tilde{s} - \beta^* \tilde{b}_y, \quad b_y^\dagger = \beta^* \tilde{s}^\dagger + \alpha \tilde{b}_y^\dagger, \quad b_y = \beta \tilde{s} + \alpha \tilde{b}_y, \quad b_x = \tilde{b}_x. \quad (12)$$

such that  $|G\rangle$  is given by

$$|G\rangle = \prod_{\mathbf{i}} \tilde{s}_i^\dagger |\emptyset\rangle. \quad (13)$$

(7) in the new basis reads (we drop the tildas for simplicity)

$$\begin{aligned} H = & \mu \sum_{\mathbf{i}} b_{\mathbf{i},x}^\dagger b_{\mathbf{i},x} - t \sum_{\mathbf{i}} \sum_{\boldsymbol{\delta}} b_{\mathbf{i}+\boldsymbol{\delta},x}^\dagger (\alpha s_{\mathbf{i}+\boldsymbol{\delta}} - \beta^* b_{\mathbf{i}+\boldsymbol{\delta},y}) (\alpha s_{\mathbf{i}}^\dagger - \beta b_{\mathbf{i},y}^\dagger) b_{\mathbf{i},x} \\ & + \mu \sum_{\mathbf{i}} (\beta^* s_{\mathbf{i}}^\dagger + \alpha b_{\mathbf{i},y}^\dagger) (\beta s_{\mathbf{i}} + \alpha b_{\mathbf{i},y}) \\ & - t \sum_{\mathbf{i}} \sum_{\boldsymbol{\delta}} (\beta^* s_{\mathbf{i}+\boldsymbol{\delta}}^\dagger + \alpha b_{\mathbf{i}+\boldsymbol{\delta},y}^\dagger) (\alpha s_{\mathbf{i}+\boldsymbol{\delta}} - \beta^* b_{\mathbf{i}+\boldsymbol{\delta},y}) (\alpha s_{\mathbf{i}}^\dagger - \beta b_{\mathbf{i},y}^\dagger) (\beta s_{\mathbf{i}} + \alpha b_{\mathbf{i},y}) \\ & + \frac{V}{2} \sum_{\mathbf{i}} \sum_{\boldsymbol{\delta}} \left( b_{\mathbf{i},x}^\dagger b_{\mathbf{i},x} + (\beta^* s_{\mathbf{i}}^\dagger + \alpha b_{\mathbf{i},y}^\dagger) (\beta s_{\mathbf{i}} + \alpha b_{\mathbf{i},y}) \right) (\mathbf{i} \rightarrow \mathbf{i} + \boldsymbol{\delta}) \\ & - \frac{J}{2} \sum_{\mathbf{i}} \sum_{\boldsymbol{\delta}} \left( b_{\mathbf{i},x}^\dagger (\beta s_{\mathbf{i}} + \alpha b_{\mathbf{i},y}) - (\beta^* s_{\mathbf{i}}^\dagger + \alpha b_{\mathbf{i},y}^\dagger) b_{\mathbf{i},x} \right) (\mathbf{i} \rightarrow \mathbf{i} + \boldsymbol{\delta}) \\ & + \frac{W}{2} \sum_{\mathbf{i}} \sum_{\boldsymbol{\delta}} \left( b_{\mathbf{i}+\boldsymbol{\delta},x}^\dagger (\alpha s_{\mathbf{i}+\boldsymbol{\delta}} - \beta^* b_{\mathbf{i}+\boldsymbol{\delta},y}) b_{\mathbf{i},x}^\dagger (\alpha s_{\mathbf{i}} - \beta^* b_{\mathbf{i},y}) + h.c. \right) \\ & + \frac{W}{2} \sum_{\mathbf{i}} \sum_{\boldsymbol{\delta}} \left( (\beta^* s_{\mathbf{i}+\boldsymbol{\delta}}^\dagger + \alpha b_{\mathbf{i}+\boldsymbol{\delta},y}^\dagger) (\alpha s_{\mathbf{i}+\boldsymbol{\delta}} - \beta^* b_{\mathbf{i}+\boldsymbol{\delta},y}) (\beta^* s_{\mathbf{i}}^\dagger + \alpha b_{\mathbf{i},y}^\dagger) (\alpha s_{\mathbf{i}} - \beta^* b_{\mathbf{i},y}) + h.c. \right). \end{aligned} \quad (14)$$

Next, we classify the new operators into  $ssss$ ,  $bsss$ ,  $bbss$ ,  $bbbs$  and  $bbbb$  and keep only those, which have non-zero action on  $|G\rangle$ . This leads to approximate non-interacting Hamiltonian describing the elementary excitations

$$\begin{aligned} \tilde{H} = & (\mu + zV|\beta|^2 - \mu_0) \sum_{\mathbf{i}} \tilde{b}_{\mathbf{i},x}^\dagger \tilde{b}_{\mathbf{i},x} - (\alpha^2 t - J|\beta|^2) \sum_{\mathbf{i}} \sum_{\boldsymbol{\delta}} \tilde{b}_{\mathbf{i}+\boldsymbol{\delta},x}^\dagger \tilde{b}_{\mathbf{i},x} \\ & + \sum_{\mathbf{i}} \sum_{\boldsymbol{\delta}} \left( \left( \frac{\alpha^2 W}{2} - \frac{\beta^2 J}{2} \right) \tilde{b}_{\mathbf{i}+\boldsymbol{\delta},x}^\dagger \tilde{b}_{\mathbf{i},x}^\dagger + H.c. \right) \\ & + (\alpha^2 \mu + 2zt\alpha^2 |\beta|^2 + zV\alpha^2 |\beta|^2 - zW\alpha^2 (\beta^2 + (\beta^*)^2) - \mu_0) \sum_{\mathbf{i}} \tilde{b}_{\mathbf{i},y}^\dagger \tilde{b}_{\mathbf{i},y} \\ & - (t(\alpha^4 + |\beta|^4) - \alpha^2 |\beta|^2 V + W\alpha^2 (\beta^2 + (\beta^*)^2)) \sum_{\mathbf{i}} \sum_{\boldsymbol{\delta}} \tilde{b}_{\mathbf{i}+\boldsymbol{\delta},y}^\dagger \tilde{b}_{\mathbf{i},y} \\ & + \sum_{\mathbf{i}} \sum_{\boldsymbol{\delta}} \left( (\alpha^2 \beta^2 (t + \frac{V}{2}) + (\alpha^4 + \beta^4) \frac{W}{2}) \tilde{b}_{\mathbf{i}+\boldsymbol{\delta},y}^\dagger \tilde{b}_{\mathbf{i},y}^\dagger + H.c. \right). \end{aligned} \quad (15)$$

$$\begin{aligned} \mu_0 = & \mu |\beta|^2 - 2zt\alpha^2 |\beta|^2 + zV|\beta|^4 + W\alpha^2 (\beta^2 + (\beta^*)^2) \\ = & \mu |\beta|^2 - 2z(t + |W|)\alpha^2 |\beta|^2 + zV|\beta|^4 \end{aligned} \quad (16)$$

The new operators are defined as  $\tilde{b}_{i\nu}^\dagger = b_{i\nu}^\dagger s_i$ . After straightforward manipulation the parameters listed in Table 1 of the main text can be obtained.

In Fig. 8 we show the dependencies of the Higgs gap and sound velocities on the parameter  $\mu$ . The model parameters are calculated from the parameters of the two-band Hubbard model using the strong coupling formulas [3]. The evolution of the two bosonic branches for various values of  $W$  is shown in the included movies.

Table II. The effective parameters for spin wave Hamiltonians. The variational parameter  $\alpha^2 = \frac{\mu+z(t+|W|)+zV}{2z(t+|W|)+zV}$  gives the fraction of LS state in the ground state.

$\mu_x$	$\alpha^2\mu + z\alpha^2(1-\alpha^2)(2t+2 W +V)$
$t_x$	$\alpha^2t - (1-\alpha^2)J$
$W_x$	$\alpha^2W + \text{sgn}(W)(1-\alpha^2)J$
$\mu_y$	$z(t+ W )$
$t_y$	$t - \alpha^2(1-\alpha^2)(2t+2 W +V)$
$W_y$	$W - \text{sgn}(W)\alpha^2(1-\alpha^2)(2t-2 W +V)$

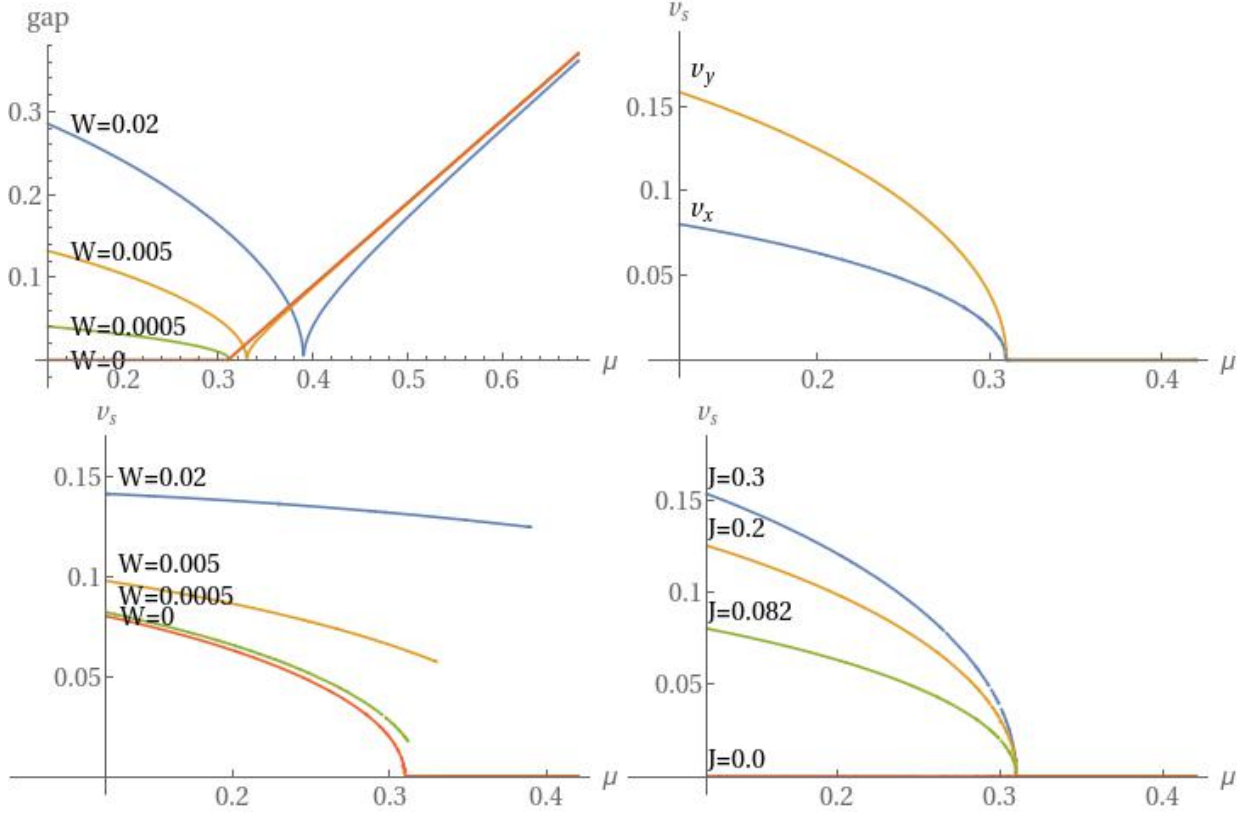


Figure 8. Dependencies of various physical characteristics on  $\mu$  (a) The gap in the spectrum of  $y$ -bosons for various values of  $W$ . (b) The sound velocity of the  $x$ -boson for various values of  $W$ . (c) The sound velocities of the  $x$  and  $y$  bosons for  $W = 0$ . (d) The sound velocity of the  $x$  bosons for  $W = 0$  for various values of  $J$ . Unless explicitly stated above in the plots we have use the parameters  $Z = 4$ ,  $t = 0.0775$ ,  $V = 0.164$ ,  $J = 0.082$ ,  $W = 0.0005$ , which correspond to the strong coupling limit [3] of the model studied in the paper.

### Goldstone modes in the $U(2)$ symmetric case

If  $W = J = 0$  the Hamiltonian (4) possesses  $U(2)$  symmetry with the standard generators

$$g_0 = b_1^\dagger b_1 + b_{-1}^\dagger b_{-1} \quad (17)$$

$$g_1 = b_1^\dagger b_{-1} + b_{-1}^\dagger b_1 \quad (18)$$

$$g_2 = -i \left( b_1^\dagger b_{-1} - b_{-1}^\dagger b_1 \right) \quad (19)$$

$$g_3 = b_1^\dagger b_1 - b_{-1}^\dagger b_{-1}, \quad (20)$$

which fulfill the commutation relations  $[g_0, g_i] = 0$  and  $[g_i, g_j] = i\varepsilon_{ijk}g_k$  ( $i, j, k > 0$ ). Let us assume the orientation of the order parameter as in the main text, i.e., given by the operator

$$\phi = b_1^\dagger + b_1 - b_{-1}^\dagger - b_{-1}. \quad (21)$$

We see that  $U(1)$  symmetry generated by  $g_0 + g_1$  is preserved ( $[\phi, g_0 + g_1] = 0$ ), while the generators  $g_0 - g_1$ ,  $g_2$  and  $g_3$  are broken. From the mutual commutators  $[g_2, g_3] = ig_1$ ,  $[g_0 - g_1, g_2] = -ig_3$ ,  $[g_0 - g_1, g_3] = ig_2$  only the first one has a non-zero expectation value. Therefore following Ref. 4 we expect one odd (linear) and one even (quadratic) Goldstone mode.

### Phase boundary

We have estimate the critical crystal field  $\Delta_c$  by matching the calculated dependence of the order parameter  $\phi(\Delta)$  with the strong-coupling expression. We find a surprisingly good match in Fig. 9, where we only shifted the strong-coupling curve by  $+0.02$  horizontally and scaled the amplitude of  $\phi$  by 1.05.

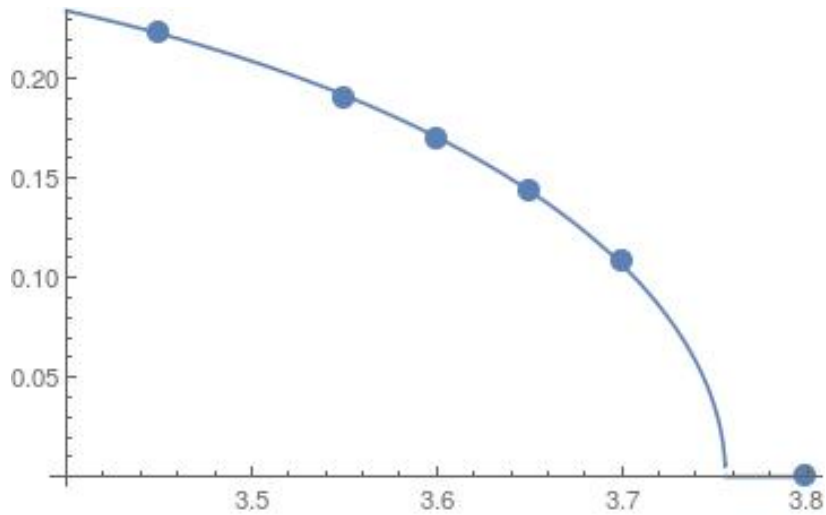


Figure 9. The calculated (DMFT) order parameter  $\phi$  as a function of crystal field  $\Delta$  (symbols) for the  $U^2(1)$  model at the inverse temperature  $\beta = 40$ . The corresponding strong-coupling results rescaled by 1.05 and horizontally shifted by  $+0.02$  (line).

### Analysis of DMFT susceptibilities

Below we show the dynamical susceptibilities of  $U^2(1)$  and  $U(1)$  models for all studied values of  $\Delta$ .

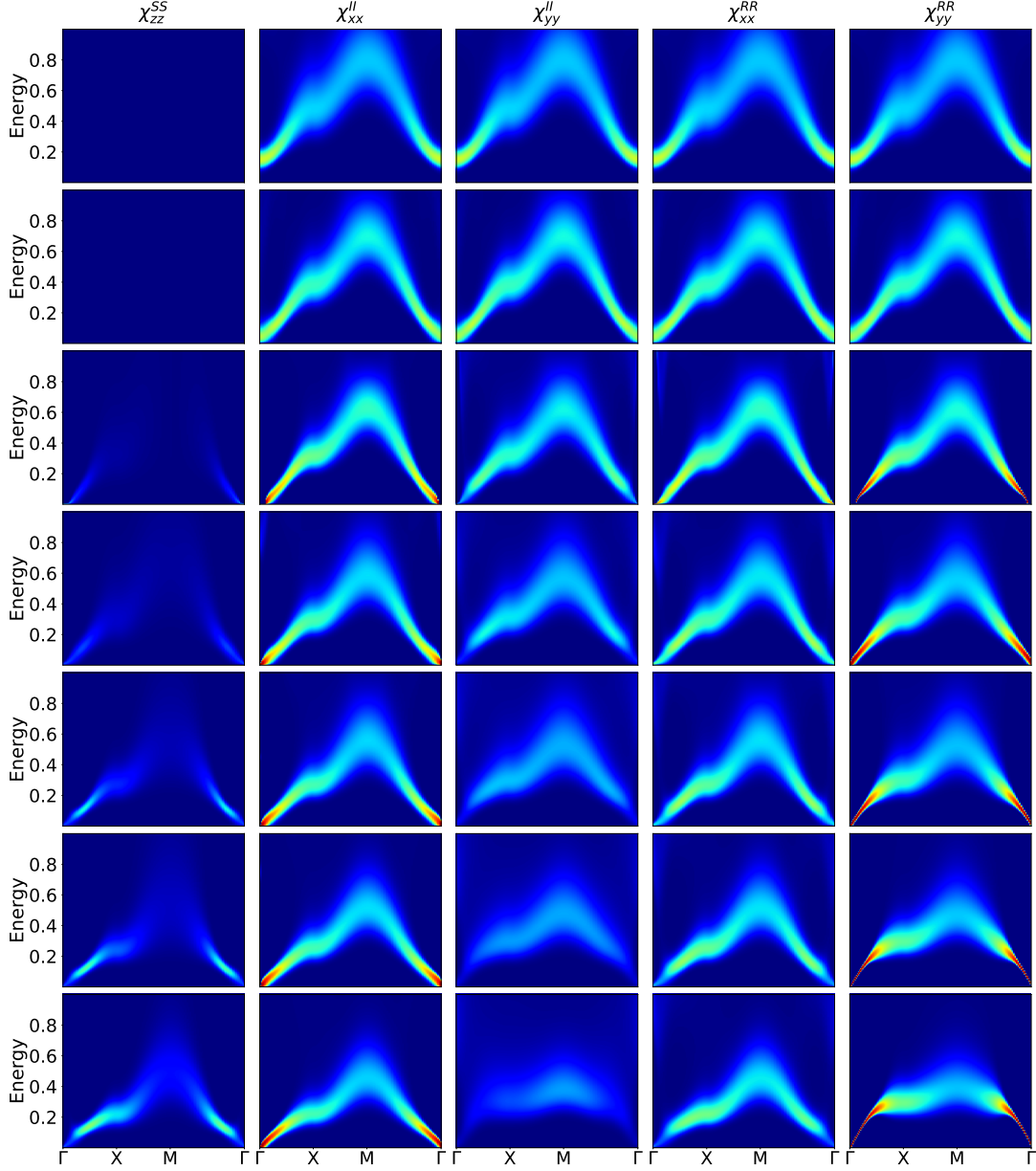


Figure 10. Evolution of the excitonic modes of the dynamical susceptibility across the low-temperature ( $T = 1/40$ ) 'quantum' phase transition driven by  $\Delta$  in the  $U^2(1)$  model ( $t_{ab}=0$ ). The columns correspond to the susceptibilities  $\chi_{\gamma\gamma}^{OO}$  with  $O^\gamma = S_z, I^x, I^y, R^x, R^y$  (left to right) along the high-symmetry lines in the 2D Brillouin zone. The rows from top to bottom correspond to  $\Delta = 3.9, 3.8, 3.7, 3.65, 3.6, 3.55, 3.45$  with  $\Delta_c \approx 3.75$ . The order parameter has the form  $\phi = (0, i)|\phi|$ .

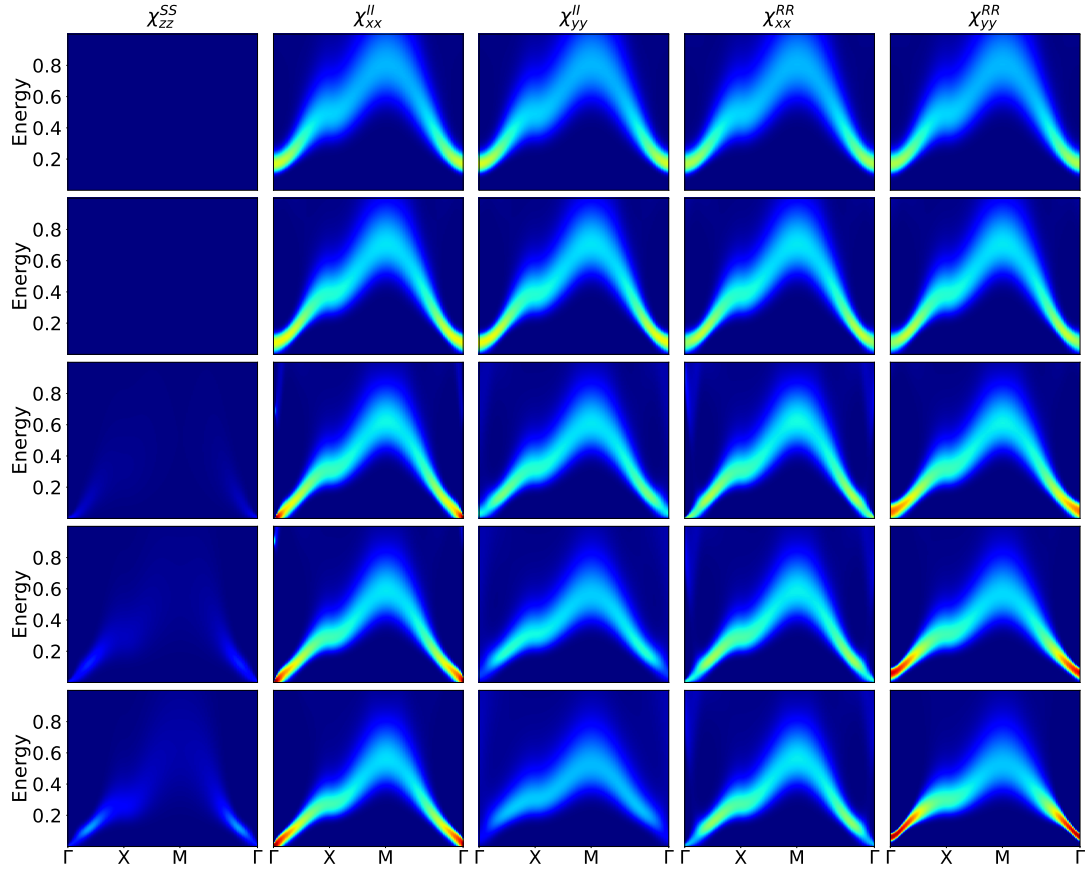


Figure 11. The same quantities as in Fig. 10, for the  $U(1)$  model with small finite cross-hopping  $t_{ab} = 0.02$ . The rows from top to bottom correspond to  $\Delta = 3.9, 3.8, 3.7, 3.65, 3.6$ , with  $\Delta_c \approx 3.75$ . The order parameter has the form  $\phi = (0, i)|\phi\rangle$ .

In Fig. 12 we show  $\chi(\mathbf{k}, \omega)$  of the  $U(1)$  model for several  $\mathbf{k}$ . Note that while the dispersions of  $\chi_{xx}^{RR}$  ( $= \chi_{yy}^{RR}$ ) and  $\chi_{xx}^{II}$  ( $= \chi_{yy}^{II}$ ) in the normal phase are identical, their amplitudes at small  $|\mathbf{k}|$  differ. This is related to the fact that the static  $\chi^{II}(0,0)$  diverges first [3] and thus the order parameter  $\phi$  is purely imaginary. In the  $U^2(1)$  the normal phase  $\chi^{RR}$  and  $\chi^{II}$  are identical and the complex phase of  $\phi$  is arbitrary.

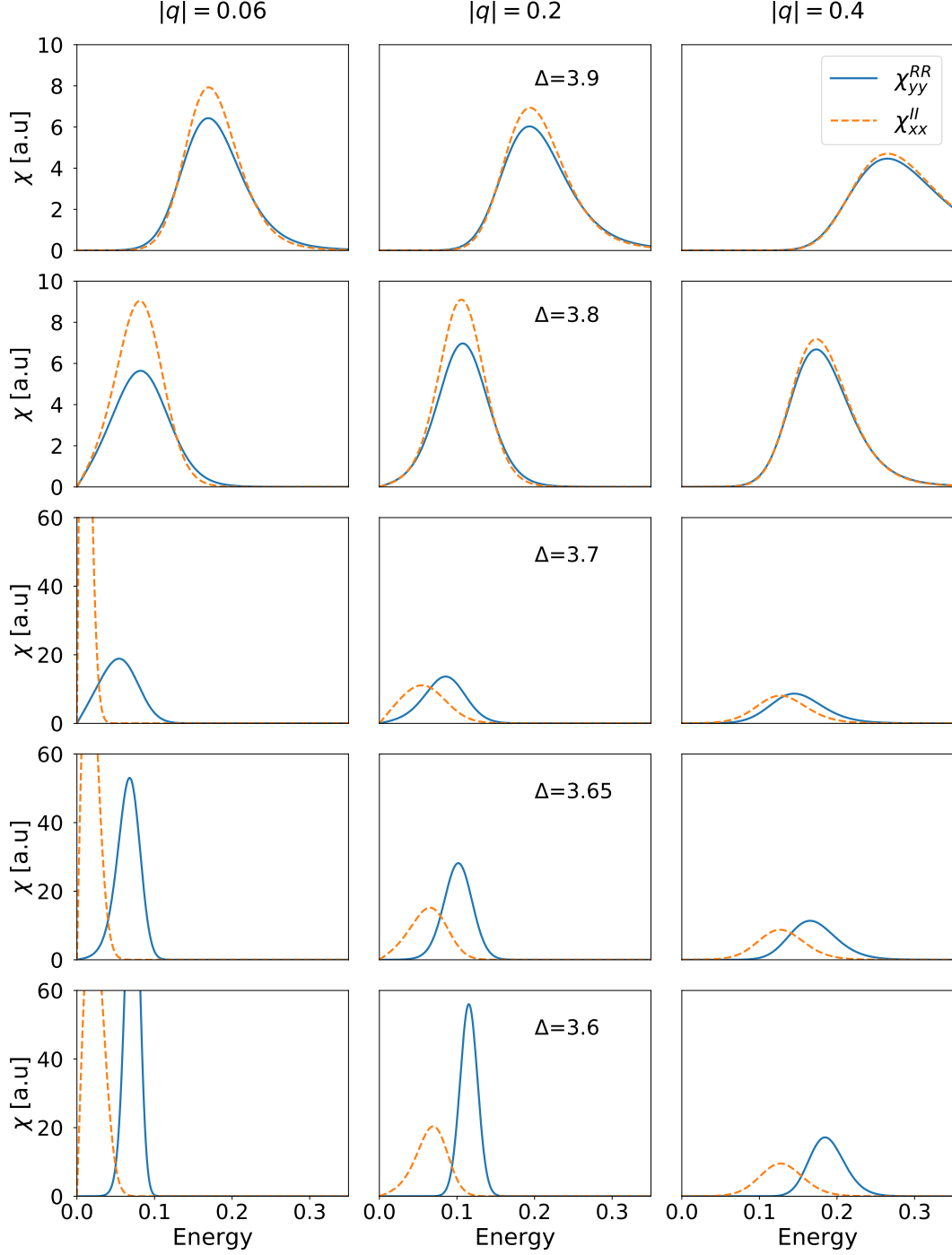


Figure 12. The profiles of  $\chi_{xx}^{II}(\mathbf{k}, \omega)$  (solid blue lines) and  $\chi_{yy}^{RR}(\mathbf{k}, \omega)$  (dashed orange line) for the  $U(1)$  model with cross-hopping  $t_{ab} = 0.02$ , for selected  $\mathbf{k}$ -points along the  $x = y$  direction.

In Fig. 13 we show the spectral weights  $SW_{\eta\eta}^{OO}(\mathbf{k}) \equiv \int_0^{\omega_c} \chi(\mathbf{k}, \omega) d\omega$ . For each  $\mathbf{k}$ -point,  $SW_{\eta\eta}^{OO}(\mathbf{k})$  is numerically evaluated using the composite trapezoidal rule implemented in the python package numpy, with  $\omega_c$  chosen larger than the bandwidth of  $\chi(\mathbf{k}, \omega)$ . The data from Fig. 13 are represented on a log-log scale in the vicinity of  $\mathbf{k} = 0$  in Fig. 14. The dashed line represents a profile  $\propto 1/|\mathbf{k}|$  for comparison.

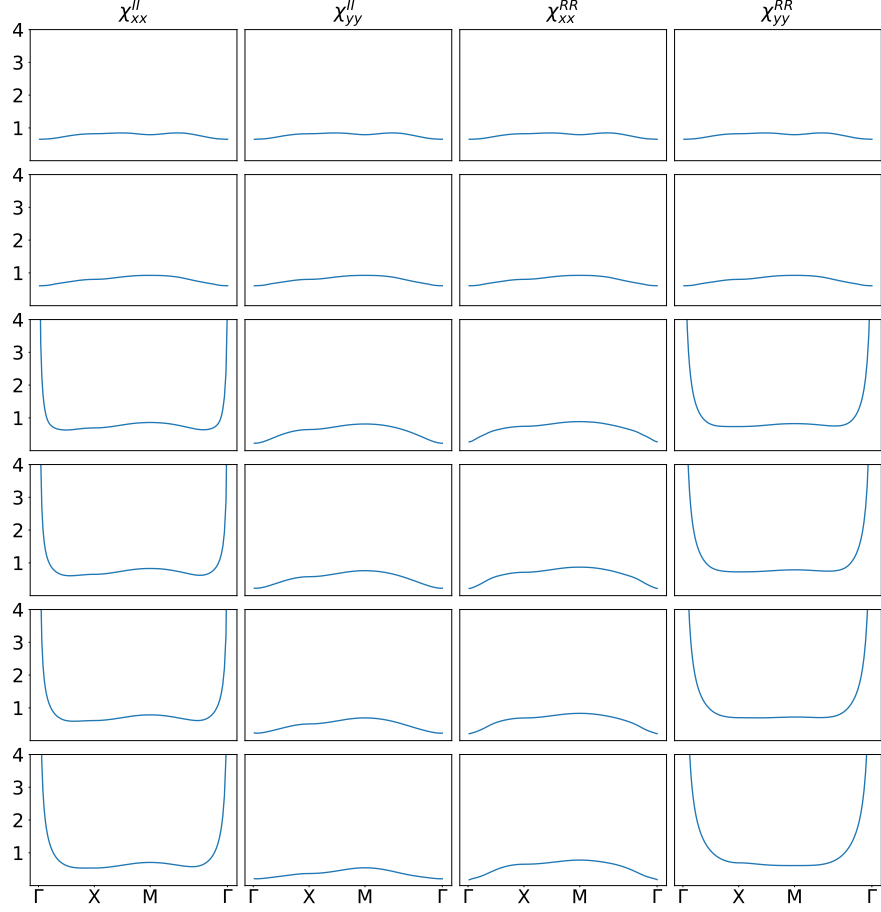


Figure 13. Evolution of the spectral weight of the excitonic modes of the dynamical susceptibility across the low-temperature ( $T = 1/40$ ) 'quantum' phase transition driven by  $\Delta$  in the  $U^2(1)$  model ( $t_{ab}=0$ ). The columns correspond to the susceptibilities  $\chi_{\gamma\gamma}^{OO}$  with  $O^\gamma = I^x, I^y, R^x, R^y$  (left to right) along the high-symmetry lines in the 2D Brillouin zone. The rows from top to bottom correspond to  $\Delta = 3.9, 3.8, 3.65, 3.6, 3.55, 3.45$  with  $\Delta_c \approx 3.75$ .

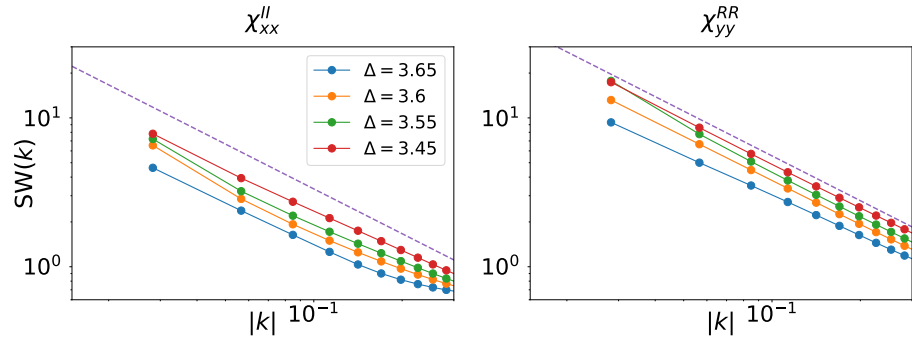


Figure 14. The same data as Fig. 13, represented on a logarithmic scale on both axes, zoomed around the  $\mathbf{k} = 0$  region of the 2D Brillouin zone. Only the Goldstone modes in the  $(1, 1)$  direction are shown. The dots represent the points where calculations were actually performed. The dashed line is a representation of a profile  $\propto 1/|\mathbf{k}|$ .

In order to determine the sound velocities (the slope of dispersion at  $\mathbf{k} = 0$ ) we have fitted the dispersion of maxima of DMFT susceptibilities with  $\varepsilon_\nu(\mathbf{k})$ , defined in the main text. (two fitting parameters). We have biased the fit with larger weights at low energy. We find overall a good match between the analytical formula and the numerical data shown in Figs. 15,16.

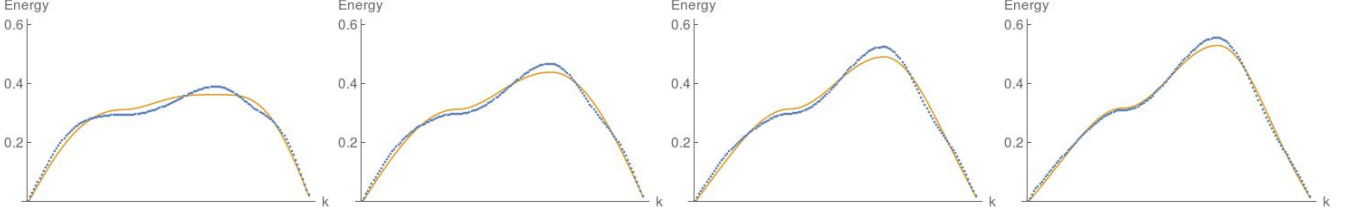


Figure 15. Maxima of  $\chi_{yy}^{RR}(\mathbf{k}, \omega)$  (point) and the two parameter fit of  $\varepsilon_\nu(\mathbf{k})$  defined in the main text (line) for  $\Delta = 3.45, 3.55, 3.60, 3.65$  used to determine the sound velocity  $v_s$ .

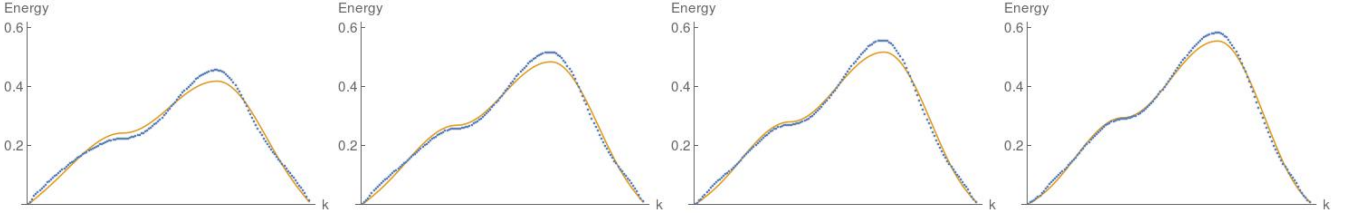


Figure 16. Maxima of  $\chi_{xx}^{II}(\mathbf{k}, \omega)$  (point) and the two parameter fit of  $\varepsilon_\nu(\mathbf{k})$  defined in the main text (line) for  $\Delta = 3.45, 3.55, 3.60, 3.65$  used to determine the sound velocity  $v_s$ .

## Analytic Continuation

### Susceptibility

The analytic continuation of susceptibilities, i. e. bosonic Green's functions, from the imaginary to the real axis is a central task of this work. To this end, a relation that connects their values on the real and imaginary axis is required. A susceptibility is a response function, therefore causality implies that its imaginary part is anti-symmetric in frequencies,  $\chi(\omega) = \chi^*(-\omega)$ . Inserting this fact in the Kramers-Kronig relation

$$\text{Re}[\chi(i\omega_n)] = \frac{1}{\pi} \int_{-\infty}^{\infty} d\omega \frac{\text{Im}[\chi(\omega)]}{\omega - i\omega_n}$$

yields

$$\text{Re}[\chi(i\omega_n)] = \frac{2}{\pi} \int_0^{\infty} d\omega \frac{\omega}{\omega^2 + \omega_n^2} \text{Im}[\chi(\omega)],$$

connecting the susceptibility at real frequencies with its values at the bosonic Matsubara frequencies  $\omega_n$ . Since the factor  $\omega/(\omega^2 + \omega_n^2)$  is divergent for  $\omega = \omega_n = 0$ , it is common to introduce another function

$$S(\omega) \equiv \frac{2}{\pi} \frac{\text{Im}\chi(\omega)}{\omega}, \quad (22)$$

such that we can now write

$$\text{Re}[\chi(i\omega_n)] = \int_0^{\infty} d\omega K_b(\omega_n, \omega) S(\omega) \quad (23)$$

with a *kernel*

$$K_b(\omega_n, \omega) = \frac{\omega^2}{\omega_n^2 + \omega^2} \quad (24)$$

that is well-defined for all values of  $\omega$  and  $\omega_n$ .

### Self-energy

Besides susceptibilities, it was also necessary calculate self-energies in real frequencies. Self-energies essentially have the same analytic properties as one-particle Green's functions [5]. The difference is that the high-frequency limit is a non-zero constant  $\Sigma_0$ , and the imaginary part decays like  $\Sigma_1/(i\omega_n)$  as opposed to  $1/(i\omega_n)$  in case of the Green's function. Note that  $\omega_n$  are fermionic Matsubara frequencies here. In absence of particle-hole symmetry, the spectral representation is

$$\Sigma(i\omega_n) = \Sigma_0 + \Sigma_1 \int_{-\infty}^{\infty} \frac{\sigma(\omega)}{i\omega_n - \omega}, \quad (25)$$

where we defined the spectrum  $\sigma$  of the self-energy as

$$\sigma(\omega) \equiv -\frac{1}{\pi} \text{Im} \frac{\Sigma(\omega) - \Sigma_0}{\Sigma_1}. \quad (26)$$

Thus, we can write the analytic continuation problem for the self-energy in a form very similar to Eq. (23):

$$\frac{\Sigma(i\omega_n) - \Sigma_0}{\Sigma_1} = \int_{-\infty}^{\infty} K_f(\omega_n, \omega) \sigma(\omega) \quad (27)$$

with the fermionic kernel

$$K_f(\omega_n, \omega) = \frac{1}{i\omega_n - \omega} \quad (28)$$

### Maximum Entropy Method

Since the numerical treatment of the problems posed in Eq. (23) and Eq. (27) is identical, we will from now on address a generic problem defined by

$$G(i\omega_n) = \int d\omega K(\omega_n, \omega) A(\omega). \quad (29)$$

A direct numerical inversion of Eq. (29) is impossible even in the presence of exact data, because the kernels of Eq. (24) and Eq. (28) have only few significant singular values. The problem is thus ill-conditioned. Consequently, many different functions  $A(\omega)$  may fulfil equation Eq. (29) equally well for a given set of data  $\chi(i\omega_n)$ , if the  $\chi^2$ -deviation

$$\chi^2[A] = 2L[A] = \sum_n \frac{(\int_0^\infty d\omega K(\omega_n, \omega) A(\omega) - \text{Re}[\chi(i\omega_n)])^2}{\sigma_n^2} \quad (30)$$

is taken as a measure for the quality of the solution. (We will use the functional  $L[A]$  from now on, in order to avoid confusion.) This means that by minimizing  $L[A]$  we do not arrive at a unique solution, and we need to add another functional that helps to select a physically meaningful one, in other words, a regularization term.

Various choices of the regularization term have been proposed [6? ], but we employ the Maximum Entropy regularization [7]. There, the functional

$$Q_\alpha[A] = L[A] - \alpha S[A] \quad (31)$$

is minimized, where the regularizing entropy

$$S[A] = \int d\omega \left[ A(\omega) - D(\omega) - A(\omega) \log \frac{A(\omega)}{D(\omega)} \right] \quad (32)$$

is scaled by a hyperparameter  $\alpha$ , and defined only with respect to a *default model*  $D(\omega)$ . It is now apparent that a critical step in the Maximum Entropy analytic continuation is the determination of an optimal value of  $\alpha$ . The most common approach utilizes Bayes' theorem, which allows to calculate the posterior probability for  $\alpha$  based on conditional probabilities (for a detailed derivation see Ref. [7]):

$$P[\alpha|G] = \int \mathcal{D}A P[G|A, \alpha] P[A|\alpha] \text{Pr}[\alpha] / \text{Pr}[G] \quad (33)$$

The notation is the following:  $P[C|B]$  is the probability of  $C$ , after  $B$  has come true, whereas  $\Pr[B]$  is the *prior* probability of  $B$ . The probability  $P[G|A, \alpha]$  is determined by the likelihood function Eq. (30),  $P[G|A, \alpha] = \exp(-L[A])/Z_L$ .  $P[A|\alpha]$  is the probability of  $A$  given  $\alpha$ , but in the absence of data. In this case only the entropy term is relevant and we have  $P[A|\alpha] = \exp(\alpha S[A])/Z_S$ .  $Z_L$  and  $Z_S$  are normalization constants. For  $\Pr[\alpha]$  we have to take the scale-invariant prior of Jeffreys,  $\Pr[\alpha] = 1/\alpha$ , whereas  $\Pr[G]$  is just a constant, and thus irrelevant. Altogether, we find

$$P[\alpha|A] = \frac{1}{\alpha} \int \mathcal{D}A \frac{e^Q}{Z_L Z_S(\alpha)} \quad (34)$$

The integration over the space of spectral functions can be carried out with a few approximations, see [7]. The approximate explicit form is then

$$\Pr[\alpha|G] = \frac{1}{\alpha} \frac{e^Q}{Z_L} \frac{\alpha^{N/2}}{\sqrt{\det(\alpha \mathbf{1} + \Lambda)}}. \quad (35)$$

Here,  $N$  is the number of real frequencies  $\omega_i$ , at which  $A(\omega)$  is sampled. The matrix  $\Lambda$  arises from the curvature of the likelihood function in the space of spectral functions:

$$\Lambda_{ij} = \sqrt{A_i} \frac{\partial^2 L}{\partial A_i \partial A_j} \sqrt{A_j} \quad (36)$$

Inserting these functions into Eq. (34), taking the logarithm, and computing the derivative with respect to  $\alpha$  leads to

$$-2\alpha S[\hat{A}_\alpha] = \sum_i \frac{\lambda_i}{\lambda_i + \alpha}. \quad (37)$$

The *classic* variant of the Maximum Entropy method iteratively minimizes Eq. (31) for various values of  $\alpha$ , until the correct value is found, i. e. Eq. (37) is fulfilled. Bryan proposed to take into account multiple solutions  $A$  by taking an average weighted by the probability of Eq. (34) [8]. However, both variants usually yield very similar results, but the classic variant requires much less computational time. In the present work, therefore, only classic Maxent is employed.

### Maxent for offdiagonal elements

The considerations above were done for positive definite spectral function with a finite norm  $\int d\omega A(\omega) > 0$ . Self-energies in the present physical system have also non-vanishing offdiagonal elements with zero norm,  $\int d\omega A(\omega) = 0$ , as a direct consequence of fermionic anticommutation relation. A vanishing norm is not consistent with a positive definite function, thus  $A$  cannot have a definite sign for offdiagonal elements. Clearly, the definition of the entropy, Eq. (32), has to be adapted to this new circumstance [9].

Let us, for offdiagonal components, write the spectrum as

$$A(\omega) = A^+(\omega) - A^-(\omega), \quad (38)$$

where both  $A^+$  and  $A^-$  are positive definite and have the same norm. Then we can write the entropy as[?] ]

$$S[A^+, A^-] = \int d\omega \left[ A^+(\omega) - D(\omega) - A^+(\omega) \log \frac{A^+(\omega)}{D(\omega)} + A^-(\omega) - D(\omega) - A^-(\omega) \log \frac{A^-(\omega)}{D(\omega)} \right] \quad (39)$$

Instead of treating  $A^+$ ,  $A^-$  and  $A$  as completely independent, we can use Eq. (38) to eliminate  $A^-$  and write

$$Q_\alpha[A, A^+] = L[A] - \alpha S[A, A^+]. \quad (40)$$

Since we are searching for a minimum of  $Q$  with respect to both  $A$  and  $A^+$ , we can use

$$\frac{\partial Q[A, A^+]}{\partial A^+} = -\alpha \frac{\partial S[A, A^+]}{\partial A^+} = 0 \quad (41)$$

to eliminate also  $A^+$ . Thus,  $A^+$  and  $A^-$ , expressed by  $A$ , are

$$A^\pm[A] = \frac{\sqrt{A^2 + 4D^2} \pm A}{2}. \quad (42)$$

Inserting this in Eq. (39), we arrive at the so-called *positive-negative entropy*

$$S^\pm[A] = \int d\omega A(\omega) \log \frac{A^+[A](\omega)}{D(\omega)}. \quad (43)$$

The different entropy in case of offdiagonal elements of matrix-valued self-energies also leads to a little difference in the determination of the maximum posterior probability for  $\alpha$ , since the matrix  $\Lambda$  now has to be defined as

$$\Lambda_{ij} = (A_i^2 + 4D_i^2)^{\frac{1}{4}} \frac{\partial^2 L}{\partial A_i \partial A_j} (A_j^2 + 4D_j^2)^{\frac{1}{4}}. \quad (44)$$

As a reasonable choice for the default model, [9] propose to include the diagonal elements of the spectrum in the following way:

$$D_{ll'} = \sqrt{A_{ll} A_{l'l'}} + \varepsilon. \quad (45)$$

In our implementation, it is not necessary to add a small number  $\varepsilon$ .

### Implementation

In the present work, we made use of the Python package `ana_cont`[? ], which contains an implementation of the Maximum entropy method. We will give a short description of the package in this section.

### Package structure

The central class of `ana_cont` is `AnalyticContinuationProblem`, which holds problem-specific information: Real-frequency grid, imaginary-frequency/time grid, data on imaginary axis, inverse temperature, and type of the kernel. It has a method `solve`, which takes several keyword arguments. The most important one is `method`. Currently, only two methods, `pade` and `maxent_svd` are implemented. Calling `solve` creates an instance of a solver object. In case of `method='maxent_svd'`, the class `MaxentSolverSVD` is instantiated. The class contains all necessary functions to solve the analytic continuation problem defined before.

Furthermore there is a class `GreensFunction`, whose main purpose is to construct a full complex-valued Green's function out of a given spectrum, by applying the Kramers-Kronig relation.

We want to stress that this package does not contain an executable script that can do analytic continuations by just specifying some parameters. While this may sound rather discouraging, we believe that in fact this *reduces* the required amount of work both for the user and for the maintainer. On the user-side, a working script can be composed of as few as 10 lines of Python code. There is full freedom in which way to provide the imaginary-axis data: They can be read from a favourite file format, or calculated on-the-fly. Computed real-axis data can be plotted or further processed without the detour of file-IO. Thus the present analytic continuation code can be easily embedded in complex postprocessing procedures. Also for the developers this principle is a large gain, since they do not have to take care of a sophisticated user interface and flow-control.

Since knowledge and experience of analytic continuation are absolutely necessary to use any analytic continuation program, we do not see a principal downside to the present approach.

### Numerics

Analytic continuation is, compared to large QMC simulations or Bethe-Salpeter equation inversions, a numerically rather inexpensive task. Therefore the performance of the code does not have to be the main goal. The `ana_cont` package is written entirely in Python, partly trading performance for flexibility and readability, while still keeping the possibility of later optimization.

Nevertheless several actions have been taken in order to make the code reasonably fast.

*Frequency-space discretization.*

For a numerical treatment it is necessary to discretize the real-frequency axis:  $\omega \rightarrow \omega_i$ . For an arbitrary function  $F(\omega)$  we then define  $F_i \equiv F(\omega_i)$ . Integrals over frequency space are converted to sums by  $\int d\omega F(\omega) \approx \sum_i F_i \Delta_i$ , where  $\Delta_i$  is the width of the frequency interval centered at  $\omega_i$ .

*Singular value decomposition.*

One of the most important steps of Maxent is the minimization of the functional  $Q_\alpha[A]$  in the space of spectral functions. If the real-frequency axis is discretized into, say, 1000 intervals, the space of solutions has 1000 dimensions. This is much too large to use a deterministic solver, and a Monte Carlo method is needed [12]. However, [7] perform a singular value decomposition of the kernel and thereby achieve a large reduction of dimensions, e. g. from 1000 to 20. The optimization method of choice is then the Levenberg-Marquart algorithm. The `MaxentSolverSVD` follows the latter strategy, and we write the singular value decomposition as

$$K_{jk} = \sum_m U_{jm} \xi_m V_{km}. \quad (46)$$

Here,  $U$  and  $V$  are quadratic matrices.  $\xi$  is the vector of singular values, which is truncated such that only values larger than a certain threshold ( $10^{-10}$  in our case) are kept. In the singular space, we parametrize the spectrum as

$$A_j = D_j \exp \sum_m V_{jm} u_m. \quad (47)$$

*Minimization problem.*

The above definitions are inserted into Eq. (31), and after a few intermediate steps the stationarity condition  $dQ/dA = 0$  leads to

$$f_m(u) \equiv \alpha u_m + \xi_m \sum_k E_k U_{km} \left( \sum_l K_{kl} A_l(u) \Delta_l - G_k \right) = 0, \quad (48)$$

which has to be solved for  $u_m$ . Root finding algorithms work better, when the derivative of the root function is known analytically. Therefore, we take the derivative of  $f$  with respect to  $u$ :

$$\frac{df_m}{du_i} \equiv J_{mi} = \alpha \delta_{mi} + \xi_m \sum_k U_{km} E_k \sum_l K_{kl} \Delta_l A_l(u) V_{li} \quad (49)$$

The expressions Eq. (48) and Eq. (49) can be put in a form that is more efficient for numerical evaluation by making the following definitions:

$$w_l \equiv \exp \left( \sum_m V_{lm} u_m \right) \quad (50a)$$

$$W_{ml} \equiv \sum_{km} E_k U_{km} \xi_m U_{kn} \xi_n V_{ln} \Delta_l D_l \quad (50b)$$

$$W_{mil} \equiv W_{ml} V_{li} \quad (50c)$$

$$B_m \equiv \sum_k U_{km} \xi_m E_k G_k \quad (50d)$$

Then we have

$$f_m = \alpha u_m + \sum_l W_{ml} w_l - B_m \quad (51a)$$

$$J_{mi} = \alpha \delta_{mi} + \sum_l W_{mil} w_l, \quad (51b)$$

where the quantities  $W_{ml}$ ,  $W_{mil}$ , and  $B_m$  are precomputed in order to minimize the number of matrix multiplications during the optimization procedure. Please note that we do *not* use the Einstein summation convention. For the optimization, the Levenberg-Marquart implementation of `scipy.optimize.root` was used.

*Offdiagonal elements.*

While the above formulas are used for susceptibilities and diagonal elements, with only very small changes we arrive at a different form that can be used for offdiagonal elements. The singular-space parametrization becomes

$$A_j = D_j \left[ \exp \left( \sum_m V_{jm} u_m \right) - \exp \left( - \sum_m \overline{V}_{jm} u_m \right) \right] = D_j (w_j - 1/w_j) \quad (52)$$

and the minimization problem is set by

$$f_m = \alpha u_m + \sum_l W_{ml} (w_l - 1/w_l) - B_m \quad (53a)$$

$$J_{mi} = \alpha \delta_{mi} + \sum_l W_{mil} (w_l + 1/w_l). \quad (53b)$$

*Hessian matrix  $\Lambda$ .*

As mentioned above, for the determination of the optimal value of  $\alpha$  we need the matrix  $\Lambda$ . Its discretized form is

$$\Lambda_{ij} = \sqrt{\frac{A_i}{\Delta_i}} \frac{\partial^2 L[A]}{\partial A_i \partial A_j} \sqrt{\frac{A_j}{\Delta_j}} = \sqrt{A_i \Delta_i} \left( \sum_k E_k K_{ki} K_{kj} \right) \sqrt{A_j \Delta_j} \quad (54)$$

for diagonal elements of Green's functions and

$$\Lambda_{ij} = (A_i^2 + 4D_i^2)^{\frac{1}{4}} \sqrt{\Delta_i} \left( \sum_k E_k K_{ki} K_{kj} \right) (A_j^2 + 4D_j^2)^{\frac{1}{4}} \sqrt{\Delta_j} \quad (55)$$

for offdiagonal elements.

*Determination of optimal  $\alpha$ .*

Previously, it has been mentioned that we are searching for  $\alpha$  in an iterative procedure. More concretely, we perform a minimization of  $Q_\alpha[A]$  for a very large value of alpha first, typically  $\log_{10}(\alpha_{\text{start}}) = 5$ . The solution of this problem is expected to be very close to the default model and we can use it as a starting point in the search for the optimal  $u$ . In every subsequent iteration,  $\alpha$  is decreased by a factor of 10, and the solution of the previous iteration is taken as a starting point. In this way, the number of function evaluations can be drastically reduced. The ratio of the right to the left side of Eq. (37) increases exponentially in this procedure. When it becomes larger than 1, the iteration is stopped and `scipy.optimize.newton` is employed to find a more precise value of  $\alpha$  [? ].

- 
- [1] T. Sommer, M. Vojta, and K. Becker, *Eur. Phys. J. B* **23**, 329 (2001).
  - [2] J. Nasu, T. Watanabe, M. Naka, and S. Ishihara, *Phys. Rev. B* **93**, 205136 (2016).
  - [3] J. Kuneš and P. Augustinský, *Phys. Rev. B* **89**, 115134 (2014).
  - [4] H. Watanabe and H. Murayama, *Phys. Rev. Lett.* **108**, 251602 (2012).
  - [5] J. M. Luttinger, *Phys. Rev.* **121**, 942 (1961).
  - [6] J. Otsuki, M. Ohzeki, H. Shinaoka, and K. Yoshimi, *Phys. Rev. E* **95**, 061302 (2017).
  - [7] M. Jarrell and J. Gubernatis, *Physics Reports* **269**, 133 (1996).
  - [8] R. K. Bryan, *European Biophysics Journal* **18**, 165 (1990).
  - [9] G. J. Kraberger, R. Triebl, M. Zingl, and M. Aichhorn, *Phys. Rev. B* **96**, 155128 (2017).
  - [10] Usually, two default models  $D^+$  and  $D^-$  are introduced, and assumed to be equal at a later point. For the sake of brevity, we omit this step.
  - [11] [https://github.com/josefkaufmann/ana\\_cont](https://github.com/josefkaufmann/ana_cont).
  - [12] A. W. Sandvik, *Phys. Rev. B* **57**, 10287 (1998).
  - [13] Strictly speaking, it is not of great importance to find the optimal  $\alpha$  with very high precision, since it's calculation is based on many approximations, and results look very similar in a certain range around it. However, the Newton root finding does not take much additional time.